Journal of Cleaner Production 428 (2023) 139359

Contents lists available at ScienceDirect

Journal of Cleaner Production

journal homepage: www.elsevier.com/locate/jclepro

Closing a biorefinery cycle of giant reed through the production of microporous and reusable activated carbon for CO_2 adsorption

Nicola Di Fidio [a,*], Domenico Licursi [a], Monica Puccini [b], Sandra Vitolo [b], Anna Maria Raspolli Galletti [a]

[a] Department of Chemistry and Industrial Chemistry, University of Pisa, Via G. Moruzzi 13, Pisa, Italy
[b] Department of Civil and Industrial Engineering, University of Pisa, Largo Lucio Lazzarino, Pisa, Italy

ARTICLE INFO

Handling editor: Maria Teresa Moreira

Keywords:
Biorefinery
Arundo donax L.
Lignin-rich residue
Activated carbon
CO_2 capture

ABSTRACT

The complete valorisation of all biomass components represents a crucial strategy for developing new biorefinery schemes. This study completed a cascade biorefinery process for the exploitation of holocellulose and lignin fractions of the non-food biomass giant reed (*Arundo donax* L.). The residual lignin-rich solid fraction, obtained after the selective conversion of hemicellulose and cellulose fractions to valuable bioproducts, was characterised and activated by KOH treatment into microporous activated carbon (AC), to be proposed for CO_2 adsorption. The production of AC was optimised by the Design of Experiments technique. Under the optimised process conditions (630 °C, KOH/lignin 3.0 wt/wt, 60 min) the AC yield was 34.4 wt% and the CO_2 uptake reached 72.3 mg/g, confirming the promising application of this biomaterial. Moreover, the obtained AC showed similar CO_2 uptake values over 10 cycles of adsorption/desorption tests, demonstrating its good recyclability, keeping its pristine CO_2 uptake capacity.

1. Introduction

The development of new biorefinery processes based on the complete exploitation of renewable resources, such as lignocellulosic biomass, is crucial for achieving most of the 17 Sustainable Development Goals defined by the United Nations (United Nations, 2023). The selective fractionation and conversion of the biomass components via chemical and/or biological routes allow the synthesis of biofuels, green solvents, biomaterials, and fine chemicals, to propose in substitution of fossil-based ones (Raspolli Galletti et al., 2021). A sustainable solution to overcome the ethical contrast "food versus fuel" consists of the use of waste or non-edible biomasses cultivated on marginal or polluted soils (Viccaro et al., 2022). Among non-edible crops, giant reed (*Arundo donax* L.) represents a suitable renewable material for developing new biorefinery schemes, since it is a perennial grass characterised by high production yield, even on marginal, contaminated, or underutilised lands, low water demand, high polysaccharide content and good resistance to several pathogens (Pilu et al., 2014; Scordia and Cosentino, 2019). Traditional biorefinery processes generally produce a lignin residue as the main side-stream, which is usually burned to produce energy with low efficiency. However, lignin represents a renewable source of aromatic compounds (Di Fidio et al., 2021b) or can be advantageously exploited through the production of new biomaterials, including activated carbon (AC) (Sellaoui et al., 2023). ACs can be proposed for the adsorption of polluting gases, such as carbon dioxide, organic compounds (Allahkarami et al., 2023b; Nandi et al., 2023; Xing et al., 2023) and polluting cations/anions in aqueous solutions, such as Ni(II), Cu(II), nitrate, etc. (Allahkarami et al., 2022; 2023a, c). The most common biorefinery models of lignocellulosic biomasses are currently developed on the cellulose exploitation, paying much lower attention to the contemporary valorisation of hemicellulose and lignin fractions.

Bio-based microporous AC has attracted much interest in recent years since it represents a sustainable and efficient adsorbent for the development of a plethora industrial applications. It is a suitable alternative to traditional adsorbents, such as organic-inorganic hybrid sorbents, zeolites, microporous polymers, and metal-organic frameworks, due to its several advantages, such as low cost, high availability, high surface area, hydrophobicity, easy recyclability, and low energy requirement for the regeneration of the pristine properties (Azmi et al., 2022; Guo et al., 2023). In particular, the wastewater treatment (WWT) of municipal and industrial effluents, and the adsorption of polluting gases represent two of the most studied AC applications. ACs are used

* Corresponding author.
E-mail address: nicola.difidio@unipi.it (N. Di Fidio).

https://doi.org/10.1016/j.jclepro.2023.139359
Received 16 July 2023; Received in revised form 27 September 2023; Accepted 16 October 2023
Available online 17 October 2023

within WWT processes due to their high efficiency in adsorbing several kinds of toxic pollutants, such as phenol and heavy metals (Allahkarami et al., 2023b; Rezai and Allahkarami, 2021). Remarkably, innovative ACs functionalised by magnetic metals have been recently employed for phenol removal from aqueous solutions, by this way improving the AC adsorption efficiency and its next recovery/reuse (Allahkarami et al., 2022a, b; 2023a).

Unfortunately, pure lignin and lignin-rich residues are generally characterised by a very low surface area, due to their macroporous or non-porous structure, thus hampering their efficient employment for adsorption uses. For this reason, a physico-chemical activation step is necessary for obtaining a microporous and functionalised texture, which is a highly desirable property for industrial applications (Alcañiz-Monge et al., 2022; Heidarinejad et al., 2020; Supanchaiyamat et al., 2019). Chemical activation offers significant advantages with respect to the physical one, since the former allows the choice of different precursors and activating agents to produce ACs in high yields and with better tailored surface properties (Alcañiz-Monge et al., 2022). Furthermore, CO_2 uptake is strictly related to the basicity of AC as well as to the activation conditions used for the biomass thermal processing (Malini et al., 2023).

The present work deals with an innovative thermochemical valorisation of the lignin-rich residue recovered at the end of a cascade process previously optimised by us for the raw *Arundo donax* L. (Di Fidio et al., 2019, 2020a). This carbon-rich biomaterial was selected as the precursor for AC production, representing the final waste of the cascade process developed for the tailored valorisation of polysaccharides, and its further valuable exploitation was proposed in the perspective of the Circular Economy criteria. In this context, the present biorefinery scheme aims at closing the circle of the complete and profitable exploitation of the starting renewable material (Fig. 1).

Fig. 1 shows the schematic representation of the cascade biorefinery implemented to obtain valuable polysaccharide derivatives and the lignin-rich residue, which was used in this work as the precursor for the production of ACs suitable for CO_2 adsorption. A tailored conversion of the holocellulose was optimised in our previous works. In the first step, the conversion of hemicellulose catalysed by $FeCl_3$ under microwave (MW) irradiation co-produced xylose and a solid residue enriched in cellulose. The latter was then used as the feedstock for the subsequent conversion of glucan to levulinic acid and formic acid catalysed again by $FeCl_3$ under MW irradiation, but working under harsher reaction conditions (Di Fidio et al., 2019, 2020a). This final lignin-rich residue represents the starting feedstock to produce AC, by using KOH as the activating agent. The process conditions for this activation treatment have been optimised by adopting the Design of Experiments (DoE) technique based on the Response Surface Modelling (RSM). The process implementation has been devoted to obtaining ACs characterised by tailored surface properties, mainly in terms of specific surface area and porosity, both highly desirable to achieve the best CO_2 adsorption.

In the literature, only a few works investigated the production of ACs directly from the raw giant reed (Bhattarai et al., 2022; Singh et al., 2017a, 2017b; Üner, 2019) while, up to now, no study considered the AC production from this lignin stream originating from such a biorefinery process. Moreover, in the literature, only two studies described the adsorption performances of AC produced by giant reed for CO_2 capture (Singh et al., 2017a, 2017b). Based on all these considerations, the main objectives of the present work were: (i) the preliminary characterisation of the starting precursor, namely the lignin-rich residue; (ii) the optimisation of the thermochemical activation of this precursor to give ACs with prevailing microporosity; (iii) the optimisation of the CO_2 uptake and the evaluation of the recycling of the most performing AC.

2. Materials and methods

2.1. Biomass and reagents

Arundo donax L. was obtained from a mature 4-year-old plantation at the Centre for Agri-environmental Research "Enrico Avanzi" of the University of Pisa, located in San Piero a Grado (Pisa, Italy). Culms and leaves were mixed and ground into particles of approximately 1.0 mm in size, then dried at 105 °C in an oven and stored in a desiccator until their utilisation. All the used chemicals were provided by Sigma-Aldrich, with the following purity degrees: water for HPLC, iron (III) chloride hexahydrate (>97%), sulfuric acid (98%), hydrochloric acid (37%), potassium bromide (≥99%), sodium hydroxide (≥98%), potassium hydroxide (90%). All reagents were used as received.

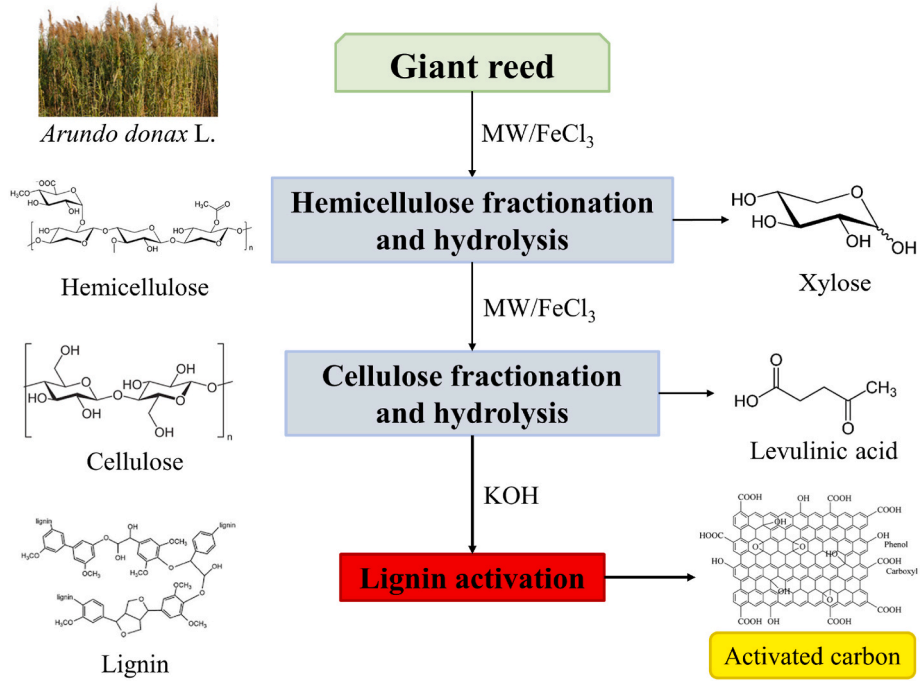

Fig. 1. Cascade biorefinery scheme developed for the complete exploitation of *Arundo donax* L.

2.2. Chemical composition of biomass samples

The chemical composition of the raw biomass and all the solid streams originating within the proposed biorefinery process was determined by the standard NREL methods (Sluiter et al., 2008). Each sample was analysed three times.

2.3. Microwave-assisted catalytic conversion

The Discover S-class microwave reactor (CEM company) was used to perform the two-step hydrolysis process of holocellulose. For the selective hydrolysis of hemicellulose to give xylose, catalysed by the homogeneous Lewis acid $FeCl_3$, the previously optimised reaction conditions were 1.5 wt% $FeCl_3$, 150 °C, 2.5 min, and 9 wt% of biomass loading (Di Fidio et al., 2019). Subsequently, for the synthesis of levulinic and formic acid from the acid-pretreated substrate, the previously optimised process conditions were 190 °C, 15 min, 2.2 wt% $FeCl_3$, and 9 wt% of biomass loading (Di Fidio et al., 2019, 2020a).

2.4. Elemental analysis

An automatic analyser Vario MICRO Cube (Elementar), equipped with a thermal conductivity detector, was used for the elemental analysis (C, H, N, S) of raw giant reed, lignin-rich residue, and AC samples. The oxygen content of the samples was calculated through equation (1):

$$O\ (wt\%) = 100\ (wt\%) - (C\ (wt\%) + H\ (wt\%) + N\ (wt\%) + S\ (wt\%) + ash\ (wt\%)) \quad (1)$$

2.5. Infrared spectroscopy

A Perkin–Elmer "Spectrum Two" spectrophotometer was used for the acquisition of IR spectra in transmission mode (KBr pellet method) and Attenuated Total Reflection (ATR) mode. In the first case, 0.5 mg of sample was mixed with 400 mg of KBr. Then 120 mg of the mixture was used for the preparation of the pellet having a thickness of 200 ± 10 μm. In the second case, the same instrument was equipped with an attenuated total reflectance apparatus. All the IR spectra were acquired through 24 scans in the range 4000-450 cm^{-1} with a nominal resolution of 8 cm^{-1}. ATR-FTIR was used for the characterisation of the raw material and lignin-rich residue (our precursor of ACs), while the transmission mode (FTIR) was used for the characterisation of ACs due to their very low transmittance.

2.6. Size-exclusion chromatography (SEC)

SEC was performed on the soluble fraction of the lignin-rich residue (accounting for 67 wt%) in an alkaline solution (0.5 M NaOH), which was used as the solvent/eluent, according to the method proposed by Constant et al. (2016). Poly (styrene sulphonate) sodium salt standards (M_w range 891–258,000 g/mol) were used for the calibration.

2.7. Synthesis of ACs

The DoE was performed according to the RSM, and it was exploited to optimise the AC synthesis from the lignin-rich residue. Activation temperature (A) and KOH/lignin weight ratio (B) were selected as the independent variables, namely the factors (Table 1). The reaction time was fixed at 60 min. For each factor, two levels (low and high) were selected, according to Table 1.

Table 1
Independent variables (factors) and levels of the experimental design.

Factor	Name	Unit	Low	High
A	Temperature	°C	500	800
B	KOH/lignin	wt/wt	3	5

The responses (dependent variables) selected to monitor the AC synthesis were: i) AC yield (wt%); ii) carbon yield (wt%); iii) CO_2 uptake (mg/g). They were calculated by the following equations:

$$Y_{AC}\ (wt\%) = (m_{AC}/m_{lignin}) \times 100 \quad (2)$$

$$Y_C\ (wt\%) = Y_{AC} \times (C\%_{AC}/C\%_{lignin}) \quad (3)$$

$$CO_2\ uptake\ (mg/g) = m_{CO2}/m_{lignin} \quad (4)$$

where Y_{AC} is the AC yield, m_{AC} is the mass of recovered AC, m_{lignin} represents the mass of the lignin-rich residue, Y_C is the carbon yield, $C\%_{AC}$ and $C\%_{lignin}$ represent the carbon content in the AC and the lignin-rich residue, respectively, determined by elemental analysis, m_{CO2} is the mass of CO_2 determined by TGA in the adsorption tests.

For the AC synthesis, the lignin-rich residue (powder) was mixed with potassium hydroxide flakes, by using an agate mortar. According to the B factor data of the DoE, 1 g of the lignin-rich residue was mixed with a proper amount of KOH, until reaching a homogenous solid mixture. For each run of the DoE, 1.25 g of the KOH/lignin mixture was transferred into an alumina cup, which was subsequently placed in a tubular reactor and heated under N_2 atmosphere (flow of 100 mL/min). The activation temperature was defined according to each run of the experimental design. The heating/cooling rate of 5 °C/min was adopted in all the tests. The solid stream recovered after pyrolysis was washed with 20 mL of 2 M HCl solution to remove the excess of KOH and with deionized water up to neutrality. AC was dried at 105 °C up to constant weight and stored in a desiccator before its use.

2.8. Thermogravimetric analysis (TGA)

The TGA of the pristine precursor and the corresponding AC was carried out by using a TGA Q500 TA Instrument. The alumina crucible containing ca. 10 mg of the sample was dynamically heated, according to the following operating conditions: i) 20 °C/min from 30 to 105 °C under a constant flow of N_2 (100% v/v); ii) 105 °C for 10 min to determine the humidity content of the sample; iii) 20 °C/min from 105 to 900 °C under a constant flow of N_2 (100% v/v); iv) 900 °C for 10 min to determine the content of organic compounds; v) cooling from 900 to 800 °C under an air/N_2 mixture flow (air 60% v/v, N_2 40% v/v); vi) 800 °C for 20 min to determine the ash content and the fixed carbon content (by difference).

2.9. CO_2 adsorption/desorption tests

The CO_2 adsorption/desorption properties of ACs were evaluated using the TGA Q500, TA Instrument. A schematic diagram of the experimental apparatus was reported in Fig. S1. The alumina crucible containing ca. 10 mg of the sample was dynamically heated under the following operating conditions: i) 20 °C/min from 27 to 105 °C under a constant flow (100 mL/min) of N_2 (100% v/v); ii) 105 °C for 10 min to remove the sample humidity; iii) from 105 to 27 °C under a constant flow (100 mL/min) of N_2 (100% v/v). The adsorption test was performed by treating the sample at 27 °C for 20 min under a 100 mL/min flow containing CO_2 60% v/v and N_2 40% v/v. After reaching the plateau, the gas flow was switched to 100 vol% N_2 (constant flow of 100 mL/min) and CO_2 desorption took place. Both during adsorption and desorption tests, the sample weight variation was acquired as a function of the time (Licursi et al., 2023).

2.10. Analysis of specific surface area, pore volume and size distribution

Multi-point determination of specific surface area, pore volume and size distribution of AC produced under different activation conditions

was performed by ALFAST company. N_2 adsorption/desorption isotherms were obtained at −196 °C by a 3Flex Adsorption Analyzer (Micrometrics). Before the analysis, a pretreatment was conducted for 180 min at 200 °C under a constant flow of N_2 (100% v/v), aimed at the humidity removal. The specific surface area of each AC was determined through the Brunauer-Emmet-Teller (BET) method, while the nonlocal density functional theory (NLDFT) was adopted for the determination of micropore size distribution, according to the literature (Jagiello et al., 2015). The BET specific surface area was evaluated taking into account the Rouquerol's theory (Rouquerol et al., 2007), which is effective for extending BET analysis to microporous materials. In this context, each microporous sample reveals an optimal range for the application of the BET fitting. In the present study, the adopted range for ACs obtained in runs 3, 6 and under the optimised conditions was withing 0.01–0.06 p/p^0, whilst for the AC obtained in run 2, it was 0.02–0.15 p/p^0. In all the performed analyses, the pressure ranges shifted downward from the typical range of the BET method, namely 0.05–0.35 p/p^0, which is notoriously an unsuitable range for microporous samples (Maziarka et al., 2021). Moreover, the Dubinin-Radushkevich model was employed for the fitting of type I isotherms.

2.11. Scanning electron microscopy (SEM)

For high-resolution imaging purposes, the SEM analysis was carried out by a FEI QUANTA 450 ESEM-FEG microscope, which operates in low vacuum mode, with a chamber vacuum pressure ranging from 10 to 130 Pa. At 30 kV, it enables a nominal electron beam resolution of 1.4 nm.

2.12. Raman spectroscopy analysis

The lignin-rich residue and AC obtained under the optimised reaction conditions were analysed by Raman spectroscopy. Raman spectra were acquired by using a Renishaw inVia confocal micro-Raman system, connected to a Leica DLML microscope equipped with a NPLAN objective (50 ×) having a numerical aperture of 0.75. The laser source was a Ng-YAG laser emitting at 532 nm, having a spectral resolution of 2.0 cm^{-1}. Positions of D and G band, FWHM and I_{DG} ratios were obtained by fitting and integrating the individual peaks with the Lorentzian function via OriginPro2023 software (R^2 value of fittings was higher than 0.98).

3. Results and discussion

3.1. Characterisation of the AC precursor

3.1.1. Analysis of chemical composition

The proposed fractionation route was developed according to a previously optimised approach, employing $FeCl_3$ as the acid catalyst and MW heating, as summarised in Fig. 1 (Di Fidio et al., 2019, 2020a). Inorganic salts are finding widespread use as green catalysts for the production of sugars, organic acids and/or furan derivatives from biomasses (Asada et al., 2020; Loow et al., 2015). Among them, $FeCl_3$ showed excellent catalytic performances for the production of monosaccharides, levulinic acid and 5-hydroxymethylfurfural from lignocellulosic and starchy biomasses (Di Fidio et al., 2020a; Iris et al., 2017). The use of MW as the heating system improves the sustainability and efficiency of the proposed biorefinery scheme because it significantly reduces the reaction time and the energy consumption (Horikoshi et al., 2017; Priecel and Lopez-Sanchez, 2018).

The chemical composition of the raw giant reed and the corresponding lignin-rich residue (constituting 21–23 wt% of the initial biomass weight, on a dry basis) obtained through the proposed two-step hydrolysis, is presented in Table 2.

The final lignin-rich residue was characterised by an almost negligible cellulose content (ca. 2.5 wt%) and a high lignin content (ca. 93 wt %), confirming the efficiency of the proposed catalytic approach for the selective cascade fractionation of the three main fractions of the lignocellulosic biomass.

Table 2
Chemical composition (wt%, on a dry basis) of raw *Arundo donax* L. and lignin-rich residue, originating from the proposed two-step hydrolysis.

Fraction	Raw *Arundo donax* L.	Lignin-rich residue
Glucan	36.3	2.6
Xylan	17.3	–
Arabinan	1.9	–
Mannan	0.6	–
Acetyl groups	3.6	–
Ash	2.0	2.9
Extractives	13.5	–
Protein	1.9	1.3
Acid-insoluble lignin	22.0	93.2
Acid-soluble lignin	0.9	–

3.1.2. ATR-FTIR spectroscopy

ATR-FTIR spectroscopy (Fig. S2) corroborated the fractionation of the hemicellulose, cellulose and lignin fractions. The absorption band at 3330 cm^{-1} is due to the stretching of the O-H group (Fiore et al., 2014), whose intensity reached its minimum in the lignin-rich residue, according to the disappearance of the holocellulose and the chemical condensation of aromatic structures characterising the lignin structure. The two absorption bands at 2920 and 2850 cm^{-1} are due to the C-H stretching vibrations of -CH_2/-CH_3 and O-CH_3, respectively (Chen et al., 2019). The absorption band at 1732 cm^{-1} is due to the C=O stretching vibrations of unconjugated ketone, carbonyl, and ester groups and it is ascribable to the acetyl groups of the hemicellulose fraction (Fiore et al., 2014). Its presence in the raw *Arundo donax* L. and its absence in the lignin-rich residue confirmed the successful hydrolysis of the hemicellulose component, as a consequence of the first hydrolysis step. Conversely, the absorption bands at 1701 and 1596 cm^{-1}, ascribed to the stretching of C=O conjugated to the aromatic rings of lignin and to the aryl ring symmetric stretching of aromatic skeletal in lignin, respectively (Chen et al., 2019), were sharper in the lignin-rich residue. Moreover, the absorption band at 1510 cm^{-1} is assessed to the asymmetric aryl ring stretching, that at 1459 cm^{-1} to the asymmetric C-H deformation, that at 1210 cm^{-1} to the C-C and C-O stretching, and that at 1110 cm^{-1} to the aromatic C-H in-plane deformation (Di Fidio et al., 2020b). Lastly, C-O stretching vibrations of hydroxyl and ether groups of cellulose are visible at 1033 cm^{-1} (Fiore et al., 2014).

3.1.3. Elemental analysis

The bulk removal of hemicellulose and cellulose from the *Arundo donax* L. biomass was also confirmed by elemental analysis. Data related to the raw biomass and the lignin-rich residue are reported in Table 3.

Carbon and oxygen contents of the lignin-rich residue were 62.0 and 33.0 wt%, respectively. These findings are consistent with previously reported literature data for major commercial lignin types, including Kraft lignin Indulin® AT, Soda Protobind™ 1000, and Alcell™ organosolv lignin (Constant et al., 2016).

3.1.4. SEC of the alkaline-soluble lignin

The molecular weight of the lignin-based precursor can significantly

Table 3
Elemental analysis of raw *Arundo donax* L. and lignin-rich residue.

Run	C (wt %)	H (wt %)	N (wt %)	O[a] (wt %)	H/C atomic ratio	O/C atomic ratio
Raw *Arundo donax* L.	46.4	5.8	0.3	45.4	1.5	0.7
Lignin-rich residue	62.0	4.8	0.2	28.6	0.9	0.3

[a] O (wt%) = 100 (wt%) – (C (wt%) + H (wt%) + N (wt%) + S (wt%) + ash (wt %)).

influence the pore ordering of the obtained AC (Qin et al., 2018). The molar mass distribution of the alkaline-soluble fraction of the lignin-rich residue (67 wt%) was determined by SEC (Fig. S3). The number average molecular weight (M_n) was 804 g/mol, while the weight average molecular weight (M_w) was 2252 g/mol. The polydispersity index (M_w/M_n) was 2.8, thus indicating a broad distribution of the biopolymer chains. These results agreed with those previously reported for *Arundo donax* L.-derived lignins (You et al., 2013) as well as for other commercial lignins (Constant et al., 2016). Remarkably, such alkaline-soluble lignin fraction could be separately exploited for the synthesis of even more added-value bio-carbons, such as ordered mesoporous carbons, by soft-template methods (Qin et al., 2018), opening the way to further valorisation routes of this residue towards various valuable chemicals and materials.

3.2. Synthesis and characterisation of AC starting from the lignin-rich residue

According to the literature, several activation methods are available, including steam activation and carbonisation coupled with gas activation, considered as physical activation methods, or chemical activation ones, requiring the impregnation with a chemical activating agent, such as KOH, H_3PO_4, $ZnCl_2$ (Azmi et al., 2022; Malini et al., 2023). There are also studies on MW-assisted activation, such as MW-assisted pyrolysis and hydrothermal carbonisation (HTC) (Kaur et al., 2021; MacDermid-Watts et al., 2021). All these methods can lead to ACs with different surface properties (mainly in terms of specific surface area and pore size distribution) and chemical composition. The choice of the most appropriate activation method depends on several factors: first of all, the final application of the AC and, secondly, the kind of the precursor (Licursi et al., 2023). In the present work, the lignin-rich residue was used as the precursor to produce cheap AC, resulting in efficient CO_2 adsorption. KOH activation is effective for the synthesis of microporous AC with a high capacity for CO_2 adsorption (Nandi et al., 2023; Singh et al., 2017a). In this context, ACs from KOH activation are characterised by a high surface area and narrow pore size distribution (Malini et al., 2023; Xing et al., 2023). The solid-to-solid reaction is effective for avoiding the carbonatation of KOH, but also for economical and practical reasons. In particular, when KOH reacts with carbon of biomass, K_2CO_3, K, H_2O, H_2, CO_2 and CO are produced, according to the following reactions (Malini et al., 2023; Nandi et al., 2023):

$$C_{(s)} + 2KOH_{(s)} + H_2O_{(l)} \rightarrow K_2CO_{3(s)} + 2H_{2(g)}$$

$$2C_{(s)} + 6KOH_{(s)} \rightarrow 2K_2CO_{3(s)} + 2K_{(s)} + 3H_{2(g)}$$

$$2C_{(s)} + 2KOH_{(s)} \rightarrow 2CO_{(g)} + 2K_{(s)} + H_{2(g)}$$

$$2C_{(s)} + 3H_2O_{(l)} \rightarrow 2CO_{(g)} + 6H_{2(g)} + 2CO_{2(g)}$$

$$C_{(s)} + CO_{2(g)} \rightarrow 2CO_{(g)}$$

$$2KOH_{(s)} \rightarrow K_2O_{(s)} + H_2O_{(g)}$$

$$KOH_{(s)} + CO_{2(g)} \rightarrow K_2CO_{3(s)} + H_2O_{(g)}$$

The production of volatiles from the precursor contributes to improve the AC porosity. In addition, the formation of pores is favoured by the following reactions, occurring mainly between biomass carbon and K_2CO_3 or K_2O (Nandi et al., 2023):

$$K_2CO_{3(s)} + 2C_{(s)} \rightarrow 2K_{(s)} + 3CO_{(g)}$$

$$K_2CO_{3(s)} + 2C_{(s)} \rightarrow K_2O_{(s)} + 2CO_{(g)}$$

$$K_2O_{(s)} + C_{(s)} \rightarrow 2K_{(s)} + 2CO_{(g)}$$

A chemometric approach based on the RSM was adopted to optimise the main process parameters of the lignin activation step (Table 4). The experimental (full-factorial randomised) test plan is shown in Table 4, including 10 total runs, with 4 runs at factorial points, 4 runs at axial points, and 2 replicates at the central point of the design, according to equation (5):

$$N_{runs} = 2^n + 2n + n_c \quad (5)$$

where N_{runs} is the number of total experimental runs required for a full-factorial central composite design (CCD), n is the number of independent factors, $2n$ is the number of axial runs and n_c is the number of runs conducted at the centre of the design. The CCD alpha value (α), which represents the distance of axial points from the centre of the design space, was set to 1.414 to obtain a rotatable design (Table 4).

The TGA curves of the precursor and ACs were acquired (Fig. S4) while the corresponding proximate analysis data are reported in Table 5.

All the ACs produced under less severe conditions ($\leq$500 °C), such as those obtained from run 5 (437.9 °C, 4.0 KOH/lignin), run 6 (500 °C, 3.0 KOH/lignin) and run 9 (500 °C, 5.0 KOH/lignin), showed the lowest fixed carbon content, which was comparable with that of the pristine lignin-rich residue (40 wt%). On the contrary, ACs synthesised at higher temperatures ($\geq$650 °C) were characterised by a higher content of fixed carbon, confirming the advanced carbonisation of the lignin-rich precursor. Moreover, most of the ACs showed a lower ash content than the maximum one (10 wt%) allowed for commercial uses (Zulkania et al., 2018).

The results of the elemental analysis of all the AC samples were reported in Table 6.

The H/C and O/C atomic ratios were reported in the van Krevelen diagram, which is useful for depicting the progress of the carbonisation progress, highlighting some details about the corresponding mechanism (Fig. 2).

The distribution of the H/C and O/C atomic ratios in the Van Krevelen diagram demonstrated that dehydration reaction was the

Table 4
Experimental design matrix (process time 60 min).

Run	T (°C)	KOH/lignin weight ratio (wt/wt)
1	862.1	4.0
2	800.0	3.0
3	650.0	2.6
4	800.0	5.0
5	437.9	4.0
6	500.0	3.0
7	650.0	5.4
8	650.0	4.0
9	500.0	5.0
10	650.0	4.0

Table 5
Proximate analysis data of precursor and ACs.

Run	Volatiles (wt%)	Fixed carbon (wt%)	Ash (wt%)
Lignin-rich residue	55.3	40.3	4.4
1	7.9	78.1	14.0
2	19.6	62.3	18.1
3	28.0	66.9	5.1
4	9.2	86.3	4.5
5	35.8	55.6	8.6
6	37.4	58.7	3.9
7	14.8	74.0	11.2
8	23.4	71.3	5.3
9	50.7	42.6	6.7
10	20.5	74.3	5.2

Table 6
Elemental analysis data of lignin-rich residue and synthesised ACs.

Run	C (wt %)	H (wt %)	N (wt %)	O[a] (wt %)	H/C atomic ratio	O/C atomic ratio
Lignin-rich residue	62.0	4.8	0.2	28.6	0.9	0.3
1	77.6	0.9	0.3	7.3	0.1	0.1
2	76.0	0.4	0.4	5.1	0.1	0.1
3	73.0	3.2	0.1	18.6	0.5	0.2
4	82.4	0.8	0.2	12.1	0.1	0.1
5	59.3	2.8	0.1	29.2	0.6	0.4
6	72.6	3.1	0.1	20.3	0.5	0.2
7	74.3	0.8	0.2	13.5	0.1	0.1
8	70.0	3.1	0.1	21.5	0.5	0.2
9	56.1	2.9	0.1	34.1	0.6	0.5
10	72.8	3.0	0.1	18.9	0.5	0.2

[a] O (wt%) = 100 (wt%) – (C (wt%) + H (wt%) + N (wt%) + S (wt%) + ash (wt %)).

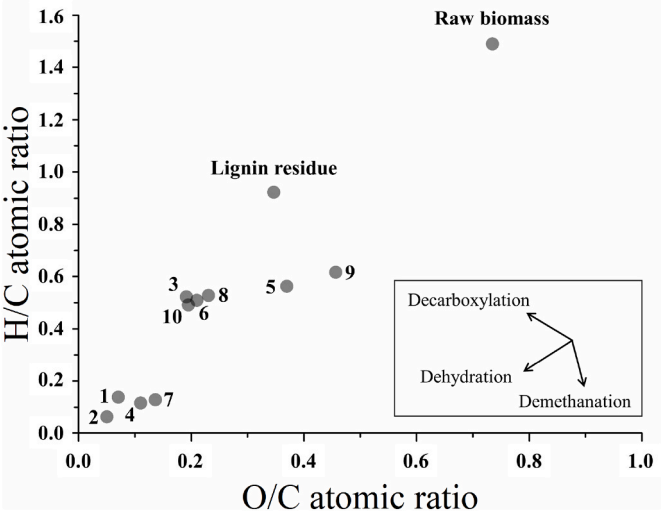

Fig. 2. Van Krevelen diagram of ACs (runs 1–10), lignin-rich residue and raw *Arundo donax* L.

prevailing path involved in the production of both lignin-rich residue and ACs. The ACs obtained at high temperatures (≥650 °C) were characterised by lower H/C and O/C atomic ratios, while those obtained under less severe conditions (≤500 °C), such as ACs obtained from runs 5 and 9, showed higher O/C values.

FTIR spectra of ACs obtained in runs 1–10 were acquired (Fig. S5). The absorption band in the range of 3100–3500 cm^{-1} is ascribable to the stretching of the O-H bonds. Those in the range 2800–3000 cm^{-1} are related to the C-H stretching vibrations of -CH_2 and -CH_3 groups. The absorption bands in the range 1000–1300 and 1640-1750 cm^{-1} are due to the stretching vibrations of C-O and C=O bonds of ketones, aldehydes and carboxylic acids, as well as phenolic esters. The intensity decrease of such absorption bands is related to the occurred removal of volatile organic compounds and the deoxygenation of the pristine material. The band at 1630 cm^{-1} is due to C=C ring stretching vibrations and it is indicative of progress of the biomass carbonisation.

The CO_2 uptake of the starting lignin-rich residue, namely the control test, and of the ACs obtained in the runs 1–10 was evaluated (Fig. S6). The AC characterised by the highest CO_2 uptake (72.6 mg/g) was obtained from run 3 (650.0 °C, KOH/lignin 2.6 wt/wt, 60 min). Moreover, by comparing the CO_2 adsorption uptake of the pristine lignin-rich residue (6.9 mg/g) and the AC, it becomes clear that the activation process significantly improved the adsorption performance. Furthermore, the use of temperatures higher than 800 °C or lower than 500 °C, together with high activating agent ratios (≥4 wt/wt), led to lower CO_2 uptakes (runs 1, 4, 5, 9, Table 6). Based on these results, intermediate activation temperatures and low KOH/lignin weight ratios were effective in improving the CO_2 uptake capacity of the ACs. Table 7 summarised the values of each response variable achieved in all the runs performed in the RSM analysis.

Table 7
Experimental data of selected response variables.

Run	AC yield (wt%)	Carbon yield (wt%)	CO_2 uptake (mg/g)
Control[a]	–	–	6.9
1	6.4	8.0	17.4
2	18.3	22.4	47.0
3	25.6	30.1	72.6
4	6.2	8.2	40.0
5	16.3	15.6	27.8
6	22.1	25.8	48.9
7	18.2	21.9	49.5
8	20.5	23.1	55.2
9	19.2	17.4	36.3
10	19.0	22.3	54.3

[a] Control test: pristine lignin-rich residue.

A mathematical model was obtained for each response variable describing the experimental domain. All the obtained models were characterised by a regression square value (R^2) higher than 0.96 and a not-significant Lack of Fit (*p*-value >0.1). The analysis of variance (ANOVA) was performed, and corresponding data were reported in Tables S1–3. Fig. 3 shows the 3D surfaces for AC and carbon yields and CO_2 uptake, respectively, as a function of the investigated process conditions.

The coded model equations related to the AC yield (wt%), carbon yield (wt%) and CO_2 uptake (mg/g) are the following:

$$Y_{AC}\,(wt\%) = 19.75 - 3.85 \times A - 3.18 \times B - 2.30 \times A \times B - 4.24 \times A^2 + 1.03 \times B^2 \quad (6)$$

$$Y_{C}\,(wt\%) = 22.70 - 2.92 \times A - 4.27 \times B - 1.45 \times A \times B - 5.56 \times A^2 + 1.54 \times B^2 \quad (7)$$

$$Y_{CO2}\,(mg/g) = 54.75 - 1.61 \times A - 6.53 \times B + 1.40 \times A \times B - 15.77 \times A^2 + 3.46 \times B^2 \quad (8)$$

The prediction of the optimal process conditions was subsequently carried out, aimed at simultaneously maximising the AC yield, the carbon yield, and the CO_2 uptake. The predicted optimal conditions were found, corresponding to an activation temperature of 630 °C and a KOH/lignin weight ratio of 3.0 wt/wt. Under these conditions, the model predicted the AC yield of 24.1 wt%, the carbon yield of 28.6 wt% and the CO_2 uptake of 64.9 mg/g (6.5 wt%). These results were experimentally validated, obtaining an AC yield of 34.4 wt%, a carbon yield of 40.6 wt% and a promising CO_2 uptake of 72.3 mg/g (7.2 wt%), confirming the effectiveness of the proposed model.

According to Song et al. (2015), commercial AC is characterised by a CO_2 adsorption capacity of around 65 mg/g (6.5 wt%) at 1 bar and 25 °C, while biomass-derived ACs show wider CO_2 uptakes, reasonably in the range 49–210 mg/g (Serafin et al., 2017). Thus, our AC produced from the *Arundo donax* L. lignin-rich residue, within the proposed biorefinery scheme, can be advantageously exploited for this application.

Raman spectra of starting lignin-rich residue and AC obtained under the optimised reaction conditions were acquired (Fig. 4).

Raman spectra of disordered and amorphous carbon exhibit two peaks at around 1340–1360 cm^{-1} (D-band) and 1570–1600 cm^{-1} (G-band), reflecting the defects in the samples and the ordered sp^2 carbon plane, respectively. The intensity ratio of the D and G band (I_{DG}) is generally considered indicative of the disorder and the graphitization degree of the carbonaceous material, whereas the values for the FWHM reflect the sizes of the domains of the different kinds of carbon structure (Yagmur et al., 2020). The parameters of interest for each deconvoluted spectrum were reported in Table 8.

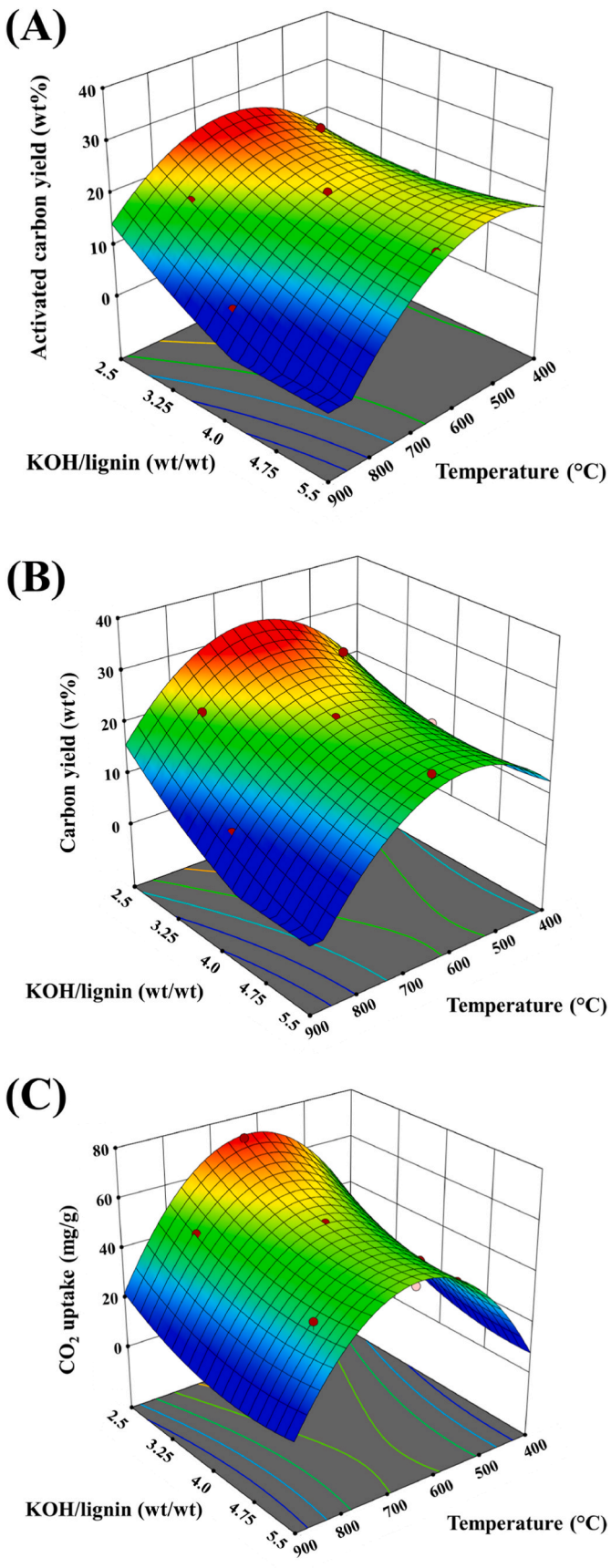

Fig. 3. Response surface of (A) AC yield (wt%), (B) carbon yield (wt%), (C) CO_2 uptake (mg/g) as a function of KOH/lignin weight ratio and temperature.

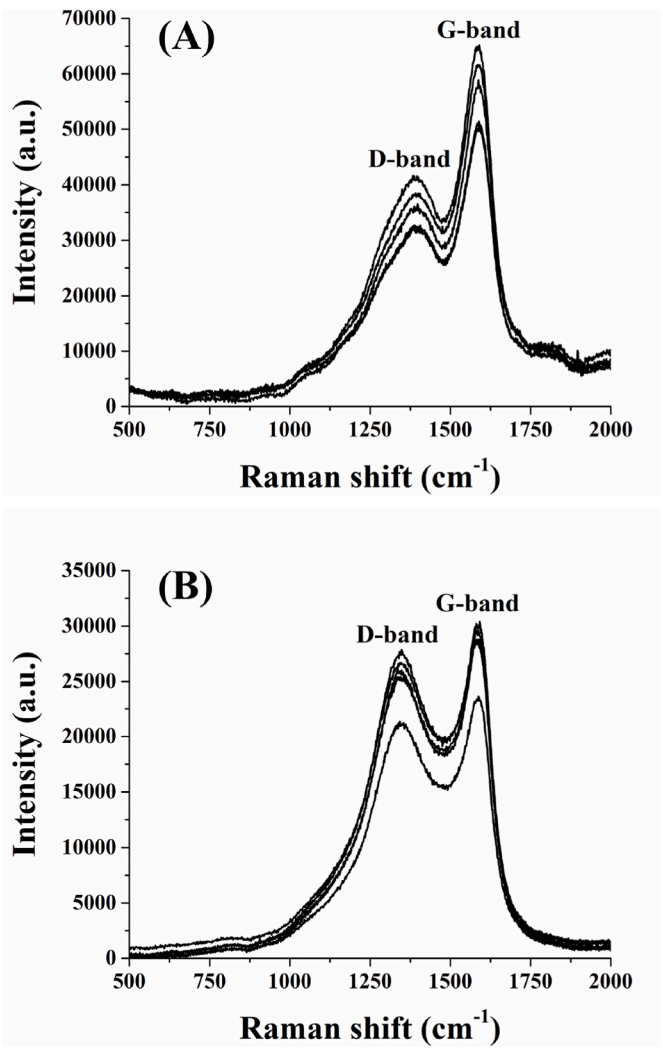

Fig. 4. Raman spectra of (A) lignin-rich residue (precursor) and (B) AC produced under the optimised conditions (630 °C, KOH/lignin 3.0 wt/wt, 60 min).

Table 8
Measured and calculated data from Raman analysis (arithmetic mean value ± standard deviation).

Sample	D pos (cm^{-1})	G pos (cm^{-1})	I_{DG}	$FWHM_D$	$FWHM_G$
Lignin-rich residue	1378 ± 5**	1587 ± 3	0.64 ± 0.02**	248 ± 8*	104 ± 2**
AC	1347 ± 3**	1588 ± 6	0.97 ± 0.02**	264 ± 4*	95 ± 3**

*$p < 0.01$; **$p < 0.001$.

The synthesised AC showed a higher I_{DG} value than that of the lignin-rich residue, suggesting the presence of more defects and a disordered graphite-like structure (i.e., a lower graphitization degree). Such a structure may be due to the intercalation of potassium and/or to the presence of oxygenated functional groups. Raman spectra of AC exhibited a strong signal for the D-mode at a decreasing position with respect to the pristine lignin-rich residue, which further confirms the disordered structure of this carbonaceous material. Higher FWHM of the D band was observed for AC, again highlighting its disordered texture. G-band FWHM is often employed to characterise carbon crystallites, and a narrower G-band FWHM implies a reduced presence of bond angle disorder in sp^2 carbons.

3.3. Analysis of specific surface area, pore volume and size distribution

N_2 adsorption isotherm linear plot and BET specific surface area plot at −196 °C of ACs obtained from run 2 (800 °C, KOH/lignin 3.0 wt/wt, 60 min), run 3 (650 °C, KOH/lignin 2.6 wt/wt, 60 min), and run 6 (500 °C, KOH/lignin 3.0 wt/wt, 60 min), corresponding to the lowest, the intermediate and the highest temperature selected in the DoE, were compared in Fig. 5. Moreover, they were compared with the AC synthesised under the optimised reaction conditions (630 °C, KOH/lignin 3.0 wt/wt, 60 min).

KOH activation promoted the selective formation of micropores, as confirmed by the type I isotherms of these ACs (Fig. 5). AC produced in the run 2 (800 °C, KOH/lignin 3.0 wt/wt) was characterised by significant microporosity and very high specific surface area, that was 2507.4 m^2/g. This specific surface area was composed of a micropore area of 2369.4 m^2/g and an external surface area of 138.0 m^2/g. AC obtained from the run 3 (650 °C, KOH/lignin 2.6 wt/wt) was also characterised by a microporous texture, with a specific surface area of 1940.4 m^2/g, whereas the micropore area was 1817.1 m^2/g and the external surface area was 123.3 m^2/g. The specific surface area of AC from run 6 (500 °C, KOH/lignin 3.0 wt/wt) was only 645.9 m^2/g, whereas the micropore area was 587.4 m^2/g and the external surface area was 58.5 m^2/g. These results confirmed that the synthesis of ACs with high microporosity is favoured by higher temperatures, in agreement with the literature (Azmi et al., 2022). The main parameters affecting the microstructure of ACs and, consequently, the N_2 gas sorption results are the type of activating agent, the impregnation ratio, and the activation temperature (Azmi et al., 2022). Regarding the activating agent, the dissolution of ether linkages of lignin-rich materials is facilitated by the utilisation of alkaline chemicals (Malini et al., 2023). Moreover, the application of an activating agent containing potassium generates additional micropores, exploiting the capacity of potassium for expanding the carbon layers. Consequently, this process enhances pore accessibility by breaking down longer fibers, favouring the production of ACs characterised by very high specific surface area and a more uniform distribution of micropores (Singh et al., 2017a). Regarding the impregnation ratio, a reduced concentration of KOH enables a more controlled and stable elimination of volatile matter while preventing the deposition of tar, thus resulting in a greater abundance of micropores (Azmi et al., 2022). Finally, the temperature employed during the activation process of carbon materials plays a crucial role in determining the pore volume, the distribution of pore sizes, the development of microporosity, and the overall specific surface area. Generally, higher temperatures facilitate the removal of moisture and volatile components from the precursor, promoting the further creation of pores (Azmi et al., 2022). However, by increasing the temperature, there is an expected significant decrease in the AC yield, along with the higher concentration of ashes, as reported in Tables 5 and 7

Under the optimised reaction conditions (630 °C, KOH/lignin 3.0 wt/wt), AC showed the specific surface area of 1848.0 m^2/g, whereas the micropore area was 1762.8 m^2/g and the external surface area was 85.2 m^2/g. As expected, these results were quite similar to those achieved from run 3. The specific surface area of 1848.0 m^2/g was significantly higher than those obtained for ACs from unpretreated *Arundo donax* L., within the range 500.0–1568.0 m^2/g (Ahmed, 2016; Singh et al., 2017a). The high specific surface area obtained in the present work further demonstrates the effectiveness of our approach.

Fig. 6 shows the cumulative surface area, the dA/dlog(W) surface area, the cumulative pore volume and the dV/dlog(W) pore volume as a function of the pore width of AC obtained from runs 2, 3, 6 and DoE validation run.

The values of the cumulative micropores volume were 1.0, 0.7, 0.2 and 0.7 cm^3/g for runs 2, 3, 6 and optimised one, respectively. For run 2 (800 °C, KOH/lignin 3.0 wt/wt), major of the micropores was characterised by a width of 9.2, 13.0 and 16.2 Å while the presence of larger micropores of around 19 Å was ascertained, as shown in Fig. 6B and D. For run 3 (650 °C, KOH/lignin 2.6 wt/wt), the most abundant micropores showed a width of 5.2, 9.1 and 13.0 Å. The AC produced in run 6 (500 °C, KOH/lignin 3.0 wt/wt) presented micropores of 5.3 and 9.6 Å. Lastly, AC obtained under the optimised reaction conditions (630 °C, KOH/lignin 3.0 wt/wt) was characterised by micropores with a width of 5.2, 9.1 and 13.0 Å, confirming the similar microporous structure and pore distribution of AC of run 3. Moreover, the micropores volume (0.7 cm^3/g) was significantly higher the those reported in the literature for AC obtained from *Arundo donax* L., ranging from 0.2 to 0.5 cm^3/g (Ahmed, 2016; Singh et al., 2017a), demonstrating again the effectiveness of the proposed cascade process.

The improvement of the CO_2 uptake requires the enhancement of the microporosity, surface area, and pore volume of the AC. Moreover, AC readily lends itself to the incorporation of surface oxygenated functional groups like carboxylates and hydroxyls, enabling CO_2 capture through processes such as cation exchange, strong complexation, and electrostatic attractions (Azmi et al., 2022). Remarkably, heteroatoms such as sulphur, nitrogen, oxygen, and hydrogen assume a crucial role by interacting specifically with CO_2, leading to improved CO_2 selectivity, and aiding in gas separation. Doping AC with oxygen or utilising raw materials rich in oxygen as precursors facilitates the creation of hydroxyl, carboxylic, and phenol functional groups, which in turn promote

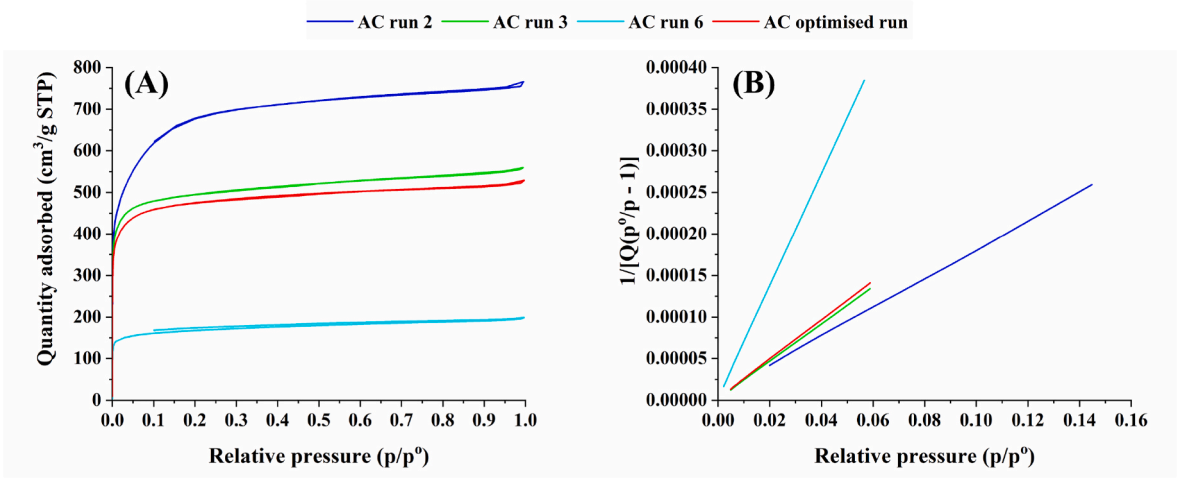

Fig. 5. (A) N_2 adsorption isotherm linear plot and (B) BET surface area plot of the AC obtained from run 2 (800 °C), run 3 (650 °C), run 6 (500 °C) and run carried out under the optimised reaction conditions (630 °C).

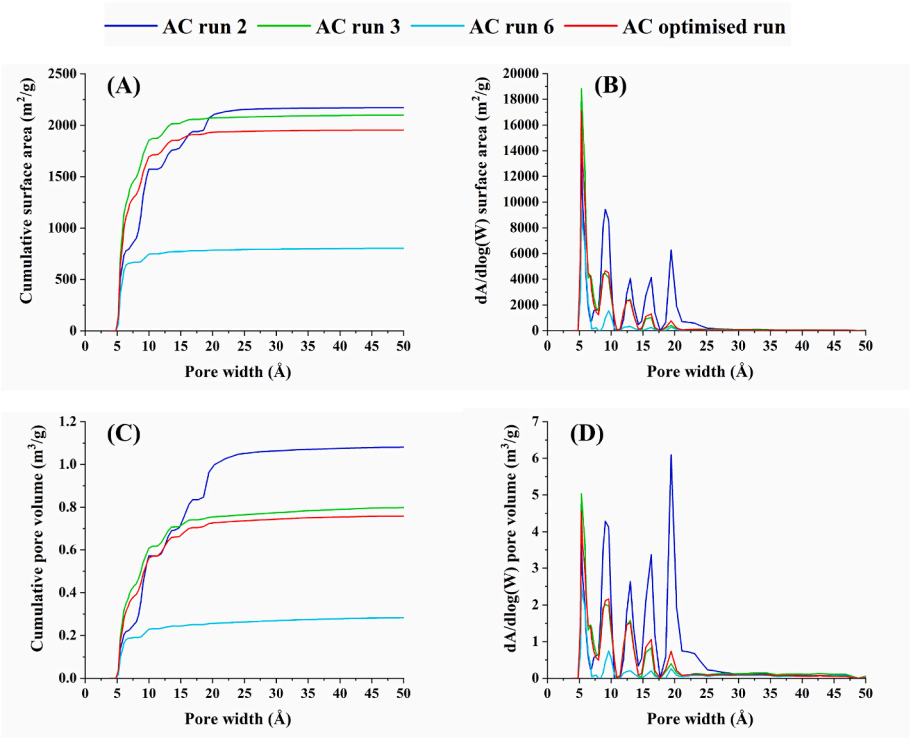

Fig. 6. Cumulative surface area (A), dA/dlog(W) surface area (B), cumulative pore volume (C) and dV/dlog(W) pore volume (D) as a function of the pore width of the AC obtained from run 2 (800 °C), run 3 (650 °C), run 6 (500 °C) and run carried out under the optimised reaction conditions (630 °C).

CO_2 capture. At the same time, a high concentration of metal oxides can result in pore clogging, ultimately diminishing the performance of CO_2 adsorption (Azmi et al., 2022). Moreover, pores below 10 Å exhibit remarkable selectivity for CO_2 molecules, when present in a N_2/CO_2 mixture (Abd et al., 2021). This selectivity arises from their ability to effectively block the passage of N_2 molecules through the pore walls. However, pores with dimensions lower than 3.5 Å show reduced adsorption performance because they approach the kinetic diameter of CO_2 molecules (3.3 Å). On the other hand, pores exceeding 10 Å in size are unsuitable for low-pressure CO_2 capture, since they may not achieve a sufficiently dense packing of CO_2 molecules (Abd et al., 2021). Once having verified the possibility of obtaining AC with a tailored microporosity, it could be possible to further improve its surface properties, depending on the physico-chemical properties of the component to be adsorbed on it. Based on these considerations, the results obtained from the analysis of the specific surface area, pore volume and size distribution of ACs produced in runs 2, 3, 6 and under the optimised conditions (Figs. 5 and 6) were correlated with those obtained from the analysis of CO_2 uptake (Table 7), as well as with those obtained from the elemental analysis (Table 6). The AC produced in run 2 (800 °C, KOH/lignin 3.0 wt/wt) was characterised by the highest values of specific surface area, micropore area, external surface area and cumulative micropores volume, but also by a lower CO_2 uptake (47.0 mg/g) with respect to the values achieved for ACs produced in run 3 (650 °C, KOH/lignin 2.6 wt/wt) and under the optimised reaction conditions (630 °C, KOH/-lignin 3.0 wt/wt), equal to 72.6 and 72.3, respectively. The better adsorbing performances of these last two ACs can be explained by considering the micropore size and distribution (Fig. 6), as well as the oxygen content (Table 6). In fact, ACs produced in run 3 and under the optimised conditions were characterised by the abundance of micropores with a width of 5.2, 9.1 and 13.0 Å and by the oxygen content of 18.6 and 18.3 wt%, respectively. Differently, AC produced in run 2 was mainly characterised by larger micropores with a width of 13.0, 16.2 and 19 Å and by a lower oxygen content (5.1 wt%) and higher ash content (18.1 wt%). The synergistic effect of these features decreased the selectivity of AC obtained in run 2 and increased that of ACs produced in run 3 and in the optimised run towards the adsorption of CO_2 molecules in the mixture CO_2/N_2, according to the literature (Abd et al., 2021). According to this reasoning, a schematic representation of the CO_2 adsorption mechanism was reported in Fig. S7.

SEM images of pristine lignin-rich precursor and AC obtained under the optimised process conditions (630 °C, KOH/lignin 3.0 wt/wt, 60 min) are shown in Fig. 7.

The effect of the thermochemical activation was evident since the lignin-rich residue was characterised by a non-porous and flat morphology while AC revealed a rather porous and shrunk structure, with pores diameter <40 μm (Fig. 7D). Moreover, as shown in Fig. 7C, AC was characterised by a uniform distribution of micropores. The morphological features of AC obtained under the optimised process conditions were ascribed to a collapse of the carbon matrix, due to the higher amount of KOH used in the activation protocol (KOH/lignin ratio of 3.0 wt/wt), in agreement with the literature findings (Singh et al., 2017a). The high concentration of KOH initiates the carbon walls' breakdown, interconnecting an aligned porous carbon structure, through oxidation at high temperature. Simultaneously, potassium residues produced during the activation process profoundly alter the surface morphology of the sample (Nandi et al., 2023). These findings underscored the importance of properly tuning the activation process of ACs, characterised by a uniform morphology, a consistently aligned porous structure, and outstanding surface properties, such as a high specific surface area and micropore volume.

3.4. *Recycling test of activated carbon for CO_2 uptake*

Fig. 8 shows 10 adsorption and desorption cycles of CO_2 by the AC obtained under the optimised process conditions.

Firstly, it is noteworthy that the maximum achieved CO_2 uptake of 72.3 mg/g was obtained by working at a CO_2 partial pressure of 0.60 bar, which is more representative of more real conditions, such as those of post-combustion flue gas. This adsorption performance demonstrated

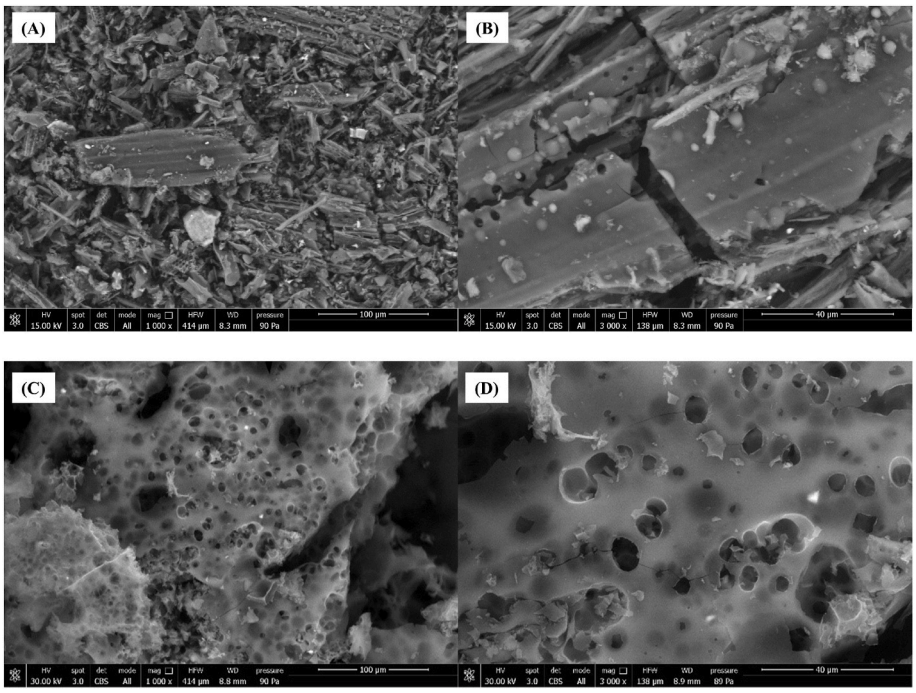

Fig. 7. SEM images of lignin-rich residue (precursor) (A, B) and AC (C, D) synthesised under the optimised process conditions identified by the RSM (630 °C, KOH/lignin 3.0 wt/wt, 60 min).

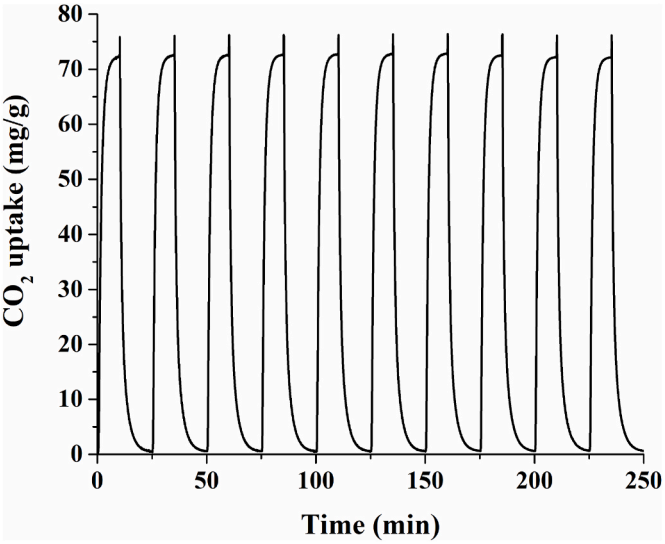

Fig. 8. CO_2 adsorption and desorption cycles by the AC obtained under the optimised activation conditions (630 °C, KOH/lignin 3.0 wt/wt, 60 min).

the feasibility of the use of this kind of AC as CO_2 adsorbent for industrial applications. Moreover, the equilibrium time observed in the recycling tests was always very short (ca. 10 min), confirming the good properties and performances of this biomaterial. Lastly, an almost identical trend was ascertained for all the cycles, thus demonstrating that the AC obtained in this study is regenerable and reusable, which are desirable aspects for eventual industrial uses. The prevailing presence of microporosity in the synthesised AC is also desirable for performing solid-liquid adsorption studies, for example, those aimed at the removal of organic pollutants, such as phenol, from wastewaters (Dehmani et al., 2023). On this basis, the use of the synthesised AC for such applications in the liquid phase seems promising and certainly worthy of further attention. These important features significantly increased the sustainability of the implemented approach for the lignin residue valorisation, especially when AC finds application as filter material (Sevilla et al., 2012).

3.5. Flow diagram of the proposed biorefinery scheme

Fig. 9 shows the mass flow diagram of the proposed biorefinery scheme, which is based on the MW-assisted conversion of hemicellulose and cellulose into xylose and levulinic acid, respectively. The subsequent step involves upgrading the xylose-rich hydrolysate (XRH) to produce single cell oil (SCO) using the yeast *L. starkeyi*, as discussed in our previous works (Di Fidio et al., 2019, 2020a, 2021a). Finally, the lignin-rich stream is valorised by producing AC under the optimised process conditions presented in this study.

Starting from 100 g of *Arundo donax* L., 19.4 g of xylose, 5.6 g of glucose, 16.7 g of levulinic acid and 18.7 g of formic acid were produced. Then, by fermenting the XRH, 4.7 g of SCO was achieved. Moreover, a final lignin-rich stream (23 g), containing 93.2 wt% acid-insoluble lignin, was obtained as the residue of this process, which allows the production of 6.4 g of AC. Lastly, it is important to emphasise the short processing time of the entire biorefinery process proposed in the present study since the first step requires only 2.5 min, the second one 15 min and the last one 60 min. The complete valorisation of the starting raw material and the sustainable reaction conditions adopted in each step significantly improved the sustainability of the cascade process in the perspective of the Green Chemistry principles.

4. Conclusions

A new thermochemical route was optimised for closing the cycle of the valorisation of *Arundo donax* L. After the hydrolysis of hemicellulose to xylose and cellulose to levulinic and formic acid, the final lignin-rich residue was characterised and chemically activated by KOH to produce AC, which was exploited for CO_2 adsorption. The chemometric approach was chosen to improve the activation protocol. Under the optimised conditions (630 °C, KOH/lignin 3.0 wt/wt, 60 min) the AC yield was 34.4 wt% and the maximum CO_2 uptake was 72.3 mg/g, kept over 10

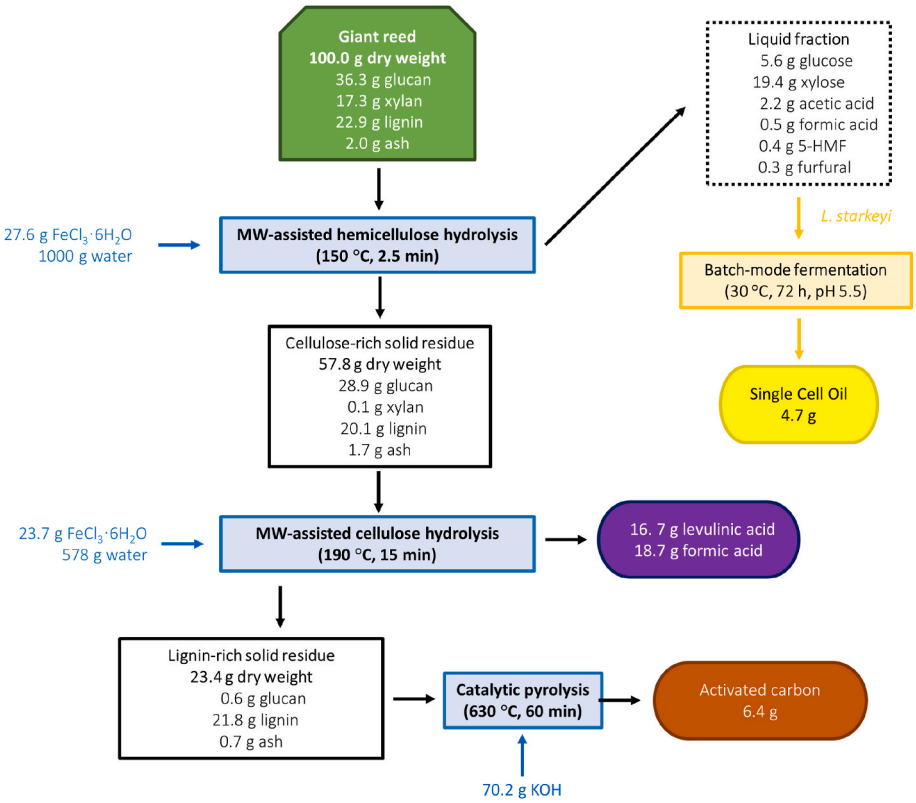

Fig. 9. Flow diagram of the cascade biorefinery process for *Arundo donax* L. exploitation.

cycles of adsorption/desorption tests, demonstrating its feasible regeneration without losing its starting CO_2 uptake capacity. The complete and tailored conversion of the different components of this non-edible biomass represents a step forward in the perspective of green and sustainable biorefinery processes.

Declaration of competing interest

The authors declare that they have no known competing financial interests or personal relationships that could have appeared to influence the work reported in this paper.

Data availability

Data will be made available on request.

Acknowledgements

Dr A. Zappavigna and Dr A. Rivellino of the company "ALFATEST Strumentazione Scientifica" are gratefully acknowledged for ACs characterisation and the support in data elaboration. I. Haaksman of the Wageningen University and Research is gratefully acknowledged for SEC analysis. Dr B. Campanella of the Consiglio Nazionale delle Ricerche is acknowledged for the Raman spectroscopy analysis. A.M. Raspolli Galletti and M. Puccini gratefully acknowledge the PRA 2020/2021 project "New horizons in CO_2 chemistry: from capture to fine chemicals and metal based drugs" (code PRA_2020_39) of the University of Pisa. N. Di Fidio acknowledges the support of the RTD-A contract (no. 1112/2021, Prot. no. 0165823/2021) co-funded by the University of Pisa in respect of the PON "Ricerca e Innovazione" 2014–2020 (PON R&I FSE-REACT EU), Azione IV.6 "Contratti di ricerca su tematiche Green".

Appendix A. Supplementary data

Supplementary data to this article can be found online at https://doi.org/10.1016/j.jclepro.2023.139359.

References

Abd, A.A., Othman, M.R., Kim, J., 2021. A review on application of activated carbons for carbon dioxide capture: present performance, preparation, and surface modification for further improvement. Environ. Sci. Pollut. Res. 28, 43329–43364. https://doi.org/10.1007/s11356-021-15121-9.

Ahmed, M.J., 2016. Potential of *Arundo donax* L. stems as renewable precursors for activated carbons and utilization for wastewater treatments. J. Taiwan Inst. Chem. Eng. 63, 336–343. https://doi.org/10.1016/j.jtice.2016.03.030.

Alcañiz-Monge, J., Román-Martínez, M.d.C., Lillo-Ródenas, M.Á., 2022. Chemical activation of lignocellulosic precursors and residues: what else to consider? Molecules 27, 1630–1655. https://doi.org/10.3390/molecules27051630.

Allahkarami, E., Azadmehr, A., Noroozi, F., Farrokhi, S., Sillanpää, M., 2022a. Nitrate adsorption onto surface-modified red mud in batch and fixed-bed column systems: equilibrium, kinetic, and thermodynamic studies. Environ. Sci. Pollut. Res. 29, 48438–48452. https://doi.org/10.1007/s11356-022-19311-x.

Allahkarami, E., Dehghan Monfared, A., Silva, L.F.O., Dotto, G.L., 2022b. Lead ferrite-activated carbon magnetic composite for efficient removal of phenol from aqueous solutions: synthesis, characterization, and adsorption studies. Sci. Rep. 12, 10718–10733. https://doi.org/10.1038/s41598-022-15077-x.

Allahkarami, E., Dehghan Monfared, A., Silva, L.F.O., Dotto, G.L., 2023a. Application of Pb–Fe spinel-activated carbon for phenol removal from aqueous solutions: fixed-bed adsorption studies. Environ. Sci. Pollut. Res. 30, 23870–23886. https://doi.org/10.1007/s11356-022-23891-z.

Allahkarami, E., Dehghan Monfared, A., Silva, L.F.O., Dotto, G.L., 2023b. Toward a mechanistic understanding of adsorption behavior of phenol onto a novel activated carbon composite. Sci. Rep. 13, 167–182. https://doi.org/10.1038/s41598-023-27507-5.

Allahkarami, E., Soleimanpour Moghadam, N., Jamrotbe, B., Azadmehr, A., 2023c. Competitive adsorption of Ni(II) and Cu(II) ions from aqueous solution by vermiculite-alginate composite: batch and fixed-bed column studies. J. Dispersion Sci. Technol. 44, 1402–1412. https://doi.org/10.1080/01932691.2021.2017297.

Asada, C., Sasaki, C., Oka, C., Nakamura, Y., 2020. Ethanol production from sugarcane bagasse using pressurized microwave treatment with inorganic salts and salt-tolerant yeast. Waste Biomass Valorization 11, 2001–2007. https://doi.org/10.1007/s12649-018-0527-z.

Azmi, N.Z.M., Buthiyappan, A., Raman, A.A.A., Patah, M.F.A., Sufian, S., 2022. Recent advances in biomass based activated carbon for carbon dioxide capture-a review. J. Ind. Eng. Chem. 116, 1–20. https://doi.org/10.1016/j.jiec.2022.08.021.

Bhattarai, K.P., Pant, B.D., Rai, R., Aryal, R.L., Paudyal, H., Gautam, S.K., Ghimire, K.N., Pokhrel, M.R., Poudel, B.R., 2022. Efficient sequestration of Cr(VI) from aqueous solution using biosorbent derived from *Arundo donax* stem. J. Chem. 2022, 1–12. https://doi.org/10.1155/2022/9926391.

Chen, B., Wang, X., Leng, W., Mei, C., Zhai, S., 2019. Spectroscopic/Microscopic elucidation for chemical changes during acid pretreatment on *Arundo donax*. J. Bioresour. Bioprod. 4, 192–199. https://doi.org/10.12162/jbb.v4i3.008.

Constant, S., Wienk, H.L., Frissen, A.E., de Peinder, P., Boelens, R., Van Es, D.S., Grisel, R. J., Weckhuysen, B.M., Huijgen, W.J., Gosselink, R.J., 2016. New insights into the structure and composition of technical lignins: a comparative characterisation study. Green Chem. 18, 2651–2665. https://doi.org/10.1039/C5GC03043A.

Dehmani, Y., Franco, D.S., Georgin, J., Lamhasni, T., Brahmi, Y., Oukhrib, R., Youcef, H. B., Sadik, A., 2023. Towards experimental and theoretical understanding of the adsorption behavior of phenol on a new activated carbon prepared from oak wood. J. Water Process Eng. 54, 103936–103947. https://doi.org/10.1016/j.jwpe.2023.103936.

Di Fidio, N., Antonetti, C., Raspolli Galletti, A.M., 2019. Microwave-assisted cascade exploitation of giant reed (*Arundo donax* L.) to xylose and levulinic acid catalysed by ferric chloride. Bioresour. Technol. 293, 122050–122058. https://doi.org/10.1016/j.biortech.2019.122050.

Di Fidio, N., Fulignati, S., De Bari, I., Antonetti, C., Raspolli Galletti, A.M., 2020a. Optimisation of glucose and levulinic acid production from the cellulose fraction of giant reed (*Arundo donax* L.) performed in the presence of ferric chloride under microwave heating. Bioresour. Technol. 313, 123650–123658. https://doi.org/10.1016/j.biortech.2020.123650.

Di Fidio, N., Ragaglini, G., Dragoni, F., Antonetti, C., Raspolli Galletti, A.M., 2021a. Integrated cascade biorefinery processes for the production of single cell oil by *Lipomyces starkeyi* from *Arundo donax* L. hydrolysates. Bioresour. Technol. 325, 124635–124645. https://doi.org/10.1016/j.biortech.2020.124635.

Di Fidio, N., Raspolli Galletti, A.M., Fulignati, S., Licursi, D., Liuzzi, F., De Bari, I., Antonetti, C., 2020b. Multi-step exploitation of raw *Arundo donax* L. for the selective synthesis of second-generation sugars by chemical and biological route. Catalysts 10, 79–101. https://doi.org/10.3390/catal10010079.

Di Fidio, N., Timmermans, J.W., Antonetti, C., Raspolli Galletti, A.M., Gosselink, R.J., Bisselink, R.J., Slaghek, T.M., 2021b. Electro-oxidative depolymerisation of technical lignin in water using platinum, nickel oxide hydroxide and graphite electrodes. New J. Chem. 45, 9647–9657. https://doi.org/10.1039/D1NJ01037A.

Fiore, V., Scalici, T., Valenza, A., 2014. Characterization of a new natural fiber from *Arundo donax* L. as potential reinforcement of polymer composites. Carbohydr. Polym. 106, 77–83. https://doi.org/10.1016/j.carbpol.2014.02.016.

Guo, B., Zhang, J., Wang, Y., Qiao, X., Xiang, J., Jin, Y., 2023. Study on CO_2 adsorption capacity and kinetic mechanism of CO_2 adsorbent prepared from fly ash. Energy 263, 125764–125775. https://doi.org/10.1016/j.energy.2022.125764.

Heidarinejad, Z., Dehghani, M.H., Heidari, M., Javedan, G., Ali, I., Sillanpää, M., 2020. Methods for preparation and activation of activated carbon: a review. Environ. Chem. Lett. 18, 393–415. https://doi.org/10.1007/s10311-019-00955-0.

Horikoshi, S., Minagawa, T., Tsubaki, S., Onda, A., Serpone, N., 2017. Is selective heating of the sulfonic acid catalyst AC-SO_3H by microwave radiation crucial in the acid hydrolysis of cellulose to glucose in aqueous media? Catalysts 7, 231–243. https://doi.org/10.3390/catal7080231.

Iris, K., Tsang, D.C., Yip, A.C., Chen, S.S., Wang, L., Ok, Y.S., Poon, C.S., 2017. Catalytic valorization of starch-rich food waste into hydroxymethylfurfural (HMF): controlling relative kinetics for high productivity. Bioresour. Technol. 237, 222–230. https://doi.org/10.1016/j.biortech.2017.01.017.

Jagiello, J., Ania, C., Parra, J.B., Cook, C., 2015. Dual gas analysis of microporous carbons using 2D-NLDFT heterogeneous surface model and combined adsorption data of N_2 and CO_2. Carbon 91, 330–337. https://doi.org/10.1016/j.carbon.2015.05.004.

Kaur, G., Singh, N., Rajor, A., 2021. Adsorption of doxycycline hydrochloride onto powdered activated carbon synthesized from pumpkin seed shell by microwave-assisted pyrolysis. Environ. Technol. Innov. 23, 101601–101614. https://doi.org/10.1016/j.eti.2021.101601.

Licursi, D., Antonetti, C., Di Fidio, N., Fulignati, S., Benito, P., Puccini, M., Vitolo, S., Raspolli Galletti, A.M., 2023. Conversion of the hydrochar recovered after levulinic acid production into activated carbon adsorbents. Waste Manage. (Tucson, Ariz.) 168, 235–245. https://doi.org/10.1016/j.wasman.2023.06.012.

Loow, Y.L., Wu, T.Y., Tan, K.A., Lim, Y.S., Siow, L.F., Md Jahim, J., Mohammad, A.W., Teoh, W.H., 2015. Recent advances in the application of inorganic salt pretreatment for transforming lignocellulosic biomass into reducing sugars. J. Agric. Food Chem. 63, 8349–8363. https://doi.org/10.1021/acs.jafc.5b01813.

MacDermid-Watts, K., Pradhan, R., Dutta, A., 2021. Catalytic hydrothermal carbonization treatment of biomass for enhanced activated carbon: a review. Waste Biomass Valorization 12, 2171–2186. https://doi.org/10.1007/s12649-020-01134-x.

Malini, K., Selvakumar, D., Kumar, N., 2023. Activated carbon from biomass: preparation, factors improving basicity and surface properties for enhanced CO_2 capture capacity–A review. J. CO_2 Util. 67, 102318–102327. https://doi.org/10.1016/j.jcou.2022.102318.

Maziarka, P., Wurzer, C., Arauzo, P.J., Dieguez-Alonso, A., Mašek, O., Ronsse, F., 2021. Do you BET on routine? The reliability of N_2 physisorption for the quantitative assessment of biochar's surface area. Chem. Eng. J. 418, 129234–129246. https://doi.org/10.1016/j.cej.2021.129234.

Nandi, R., Jha, M.K., Guchhait, S.K., Sutradhar, D., Yadav, S., 2023. Impact of KOH activation on rice husk derived porous activated carbon for carbon capture at flue gas alike temperatures with high CO_2/N_2 selectivity. ACS Omega 8, 4802–4812. https://doi.org/10.1021/acsomega.2c06955.

Pilu, R., Cassani, E., Landoni, M., Badone, F.C., Passera, A., Cantaluppi, E., Corno, L., Adani, F., 2014. Genetic characterization of an Italian Giant Reed (*Arundo donax* L.) clones collection: exploiting clonal selection. Euphytica 196, 169–181. https://doi.org/10.1007/s10681-013-1022-z.

Priecel, P., Lopez-Sanchez, J.A., 2018. Advantages and limitations of microwave reactors: from chemical synthesis to the catalytic valorization of biobased chemicals. ACS Sustain. Chem. Eng. 7, 3–21. https://doi.org/10.1021/acssuschemeng.8b03286.

Qin, H., Jian, R., Bai, J., Tang, J., Zhou, Y., Zhu, B., Zhao, D., Ni, Z., Wang, L., Liu, W., 2018. Influence of molecular weight on structure and catalytic characteristics of ordered mesoporous carbon derived from lignin. ACS Omega 3, 1350–1356. https://doi.org/10.1021/acsomega.7b01870.

Raspolli Galletti, A.M., Licursi, D., Ciorba, S., Di Fidio, N., Coccia, V., Cotana, F., Antonetti, C., 2021. Sustainable exploitation of residual *Cynara cardunculus* L. to levulinic acid and *n*-butyl levulinate. Catalysts 11, 1082–1099. https://doi.org/10.3390/catal11091082.

Rezai, B., Allahkarami, E., 2021. Wastewater treatment processes—techniques, technologies, challenges faced, and alternative solutions. In: Karri, R.R., Ravindran, G., Dehghani, M.H. (Eds.), Soft Computing Techniques in Solid Waste and Wastewater Management. Elsevier, pp. 35–53. https://doi.org/10.1016/B978-0-12-824463-0.00004-5.

Rouquerol, J., Llewellyn, P., Rouquerol, F., 2007. Is the BET equation applicable to microporous adsorbents? Stud. Surf. Sci. Catal. 160, 49–56. https://doi.org/10.1016/S0167-2991(07)80008-5.

Scordia, D., Cosentino, S.L., 2019. Perennial energy grasses: resilient crops in a changing European agriculture. Agriculture 9, 169–187. https://doi.org/10.3390/agriculture9080169.

Sellaoui, L., Gómez-Avilés, A., Dhaouadi, F., Bedia, J., Bonilla-Petriciolet, A., Rtimi, S., Belver, C., 2023. Adsorption of emerging pollutants on lignin-based activated carbon: analysis of adsorption mechanism via characterization, kinetics and equilibrium studies. Chem. Eng. J. 452, 139399–139407. https://doi.org/10.1016/j.cej.2022.139399.

Serafin, J., Narkiewicz, U., Morawski, A.W., Wróbel, R.J., Michalkiewicz, B., 2017. Highly microporous activated carbons from biomass for CO_2 capture and effective micropores at different conditions. J. CO_2 Util. 18, 73–79. https://doi.org/10.1016/j.jcou.2017.01.006.

Sevilla, M., Falco, C., Titirici, M.M., Fuertes, A.B., 2012. High-performance CO_2 sorbents from algae. RSC Adv. 2 (33), 12792–12797. https://doi.org/10.1039/C2RA22552B.

Singh, G., Kim, I.Y., Lakhi, K.S., Srivastava, P., Naidu, R., Vinu, A., 2017a. Single step synthesis of activated bio-carbons with a high surface area and their excellent CO_2 adsorption capacity. Carbon 116, 448–455. https://doi.org/10.1016/j.carbon.2017.02.015.

Singh, G., Lakhi, K.S., Kim, I.Y., Kim, S., Srivastava, P., Naidu, R., Vinu, A., 2017b. Highly efficient method for the synthesis of activated mesoporous biocarbons with extremely high surface area for high-pressure CO_2 adsorption. ACS Appl. Mater. Interfaces 9, 29782–29793. https://doi.org/10.1021/acsami.7b08797.

Sluiter, A., Hames, B., Ruiz, R., Scarlata, C., Sluiter, J., Templeton, D., Crocker, D., 2008. NREL/TP-510–42618 1617, pp. 1–16.

Song, T., Liao, J.M., Xiao, J., Shen, L.H., 2015. Effect of micropore and mesopore structure on CO_2 adsorption by activated carbons from biomass. N. Carbon Mater. 30, 156–166. https://doi.org/10.1016/S1872-5805(15)60181-0.

Supanchaiyamat, N., Jetsrisuparb, K., Knijnenburg, J.T., Tsang, D.C., Hunt, A., 2019. Lignin materials for adsorption: current trend, perspectives and opportunities. Bioresour. Technol. 272, 570–581. https://doi.org/10.1016/j.biortech.2018.09.139.

Üner, O., 2019. Hydrogen storage capacity and methylene blue adsorption performance of activated carbon produced from *Arundo donax*. Mater. Chem. Phys. 237, 121858–121868. https://doi.org/10.1016/j.matchemphys.2019.121858.

United Nations, 2023. Sustainable Development Golas. https://www.un.org/sustainabledevelopment/. (Accessed 30 August 2023).

Viccaro, M., Caniani, D., Masi, S., Romano, S., Cozzi, M., 2022. Biofuels or not biofuels? The "Nexus Thinking" in land suitability analysis for energy crops. Renew. Energy 187, 1050–1064. https://doi.org/10.1016/j.renene.2022.02.008.

Xing, L.A., Yang, F., Zhong, X., Liu, Y., Lu, H., Guo, Z., Lv, G., Yang, J., Yuan, A., Pan, J., 2023. Ultra-microporous cotton fiber-derived activated carbon by a facile one-step chemical activation strategy for efficient CO_2 adsorption. Sep. Purif. Technol. 324, 124470–124480. https://doi.org/10.1016/j.seppur.2023.124470.

Yagmur, E., Gokce, Y., Tekin, S., Semerci, N.I., Aktas, Z., 2020. Characteristics and comparison of activated carbons prepared from oleaster (*Elaeagnus angustifolia* L.) fruit using KOH and $ZnCl_2$. Fuel 267, 117232–117239. https://doi.org/10.1016/j.fuel.2020.117232.

You, T.T., Mao, J.Z., Yuan, T.Q., Wen, J.L., Xu, F., 2013. Structural elucidation of the lignins from stems and foliage of *Arundo donax* Linn. J. Agric. Food Chem. 61, 5361–5370. https://doi.org/10.1021/jf401277v.

Zulkania, A., Hanum, G.F., Rezki, A.S., 2018. The Potential of Activated Carbon Derived from Bio-Char Waste of Bio-Oil Pyrolysis as Adsorbent. MATEC Web of Conferences. EDP Sciences. https://doi.org/10.1051/matecconf/201815401029, 01029-01034.